Chemical Engineering Journal 328 (2017) 599–608

Contents lists available at ScienceDirect

Chemical Engineering Journal

journal homepage: www.elsevier.com/locate/cej

Confined growth of uniformly dispersed $NiCo_2S_4$ nanoparticles on nitrogen-doped carbon nanofibers for high-performance asymmetric supercapacitors

Xueliang Ning [a], Fei Li [a], Yu Zhou [a], Yue-E Miao [a,*], Chun Wei [b], Tianxi Liu [a,*]

[a] State Key Laboratory for Modification of Chemical Fibers and Polymer Materials, College of Materials Science and Engineering, Donghua University, 2999 North Renmin Road, Shanghai 201620, PR China

[b] Key Laboratory of New Processing Technology for Nonferrous Metals and Materials, Ministry of Education, College of Materials Science and Engineering, Guilin University of Technology, Guilin 541004, PR China

HIGHLIGHTS

- Nitrogen-doped carbon nanofiber supported $NiCo_2S_4$ composite has been fabricated.
- Highly dispersed $NiCo_2S_4$ nanoparticles are obtained with size of only 3–5 nm.
- The composite electrode shows excellent specific capacitance and cycling stability.

GRAPHICAL ABSTRACT

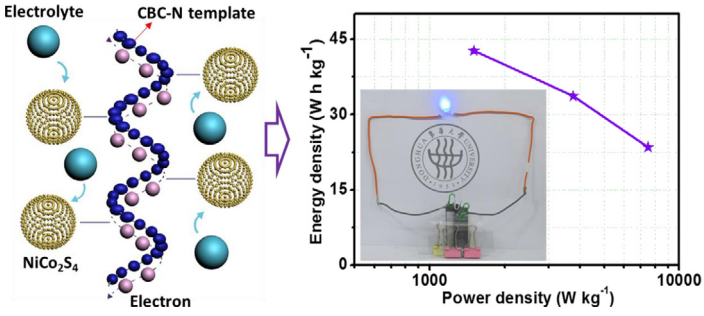

ARTICLE INFO

Article history:
Received 11 May 2017
Received in revised form 24 June 2017
Accepted 11 July 2017
Available online 12 July 2017

Keywords:
Confined growth
Ultradispersed $NiCo_2S_4$ nanoparticles
Nitrogen-doped carbon nanofibers
Asymmetric supercapacitors

ABSTRACT

To pursue high-performance energy storage devices with both high energy density and power density, nitrogen-doped carbon nanofibers (CBC-N) derived from bacterial cellulose are used both as a three-dimensional template for space-confined hydrothermal growth of $NiCo_2S_4$, and as the highly conductive negative electrode material for asymmetric supercapacitor assembly. Notably, uniformly dispersed $NiCo_2S_4$ nanoparticles with only 3–5 nm are successfully immobilized on the surface of CBC-N fibers to form the CBC-N@$NiCo_2S_4$ composite, which effectively prevents the severe aggregation of $NiCo_2S_4$ nanoparticles and fully utilizes the outstanding electrochemical activity and capacity of $NiCo_2S_4$ as the pseudocapacitive electrode material. Benefiting from the conductive CBC-N fiber template with hierarchical architectures and its coupling with uniformly dispersed $NiCo_2S_4$ nanoparticles, the CBC-N@$NiCo_2S_4$ composite exhibits high capacitance of 1078 F g^{-1} at 1 A g^{-1} and excellent capacity retention of 94.6% (918.5 F g^{-1} at 5 A g^{-1}). Furthermore, the asymmetric supercapacitor demonstrates high energy density of 42.6 Wh kg^{-1} at power density of 1500 W kg^{-1}, and long-term cycling stability of 96.8% retention after 5000 cycles. Therefore, this work provides a new strategy to develop biomass-derived high-performance electrode materials for potential applications in supercapacitors.

1. Introduction

Among various energy storage devices, supercapacitors have attract tremendous attention due to their significant advantages

* Corresponding authors.
E-mail addresses: yuee_miao@dhu.edu.cn (Yue-E Miao), txliu@dhu.edu.cn, txliu@fudan.edu.cn (T. Liu).

http://dx.doi.org/10.1016/j.cej.2017.07.062
1385-8947/

over rechargeable batteries in terms of high power density and long cycle lifetime for applications as backup/auxiliary power sources of electric vehicles and stand-by power systems [1–3]. However, supercapacitors usually exhibit lower energy densities ($\leq$10 Wh kg^{-1}) than rechargeable batteries [4,5]. Therefore, improving the energy density of supercapacitors without sacrificing their power density and cycle life still remains a great challenge.

Pseudocapacitors, consisting of transitional metal oxides/hydroxides (*e.g.*, MnO_2, $NiCo_2O_4$, $Ni(OH)_2$, $Co(OH)_2$) and $MnMoO_4$ [6–12] and conducting polymers (*e.g.*, polyaniline and polypyrrole (PPy)) [13–15], are reported to possess high specific capacitance and energy density due to their fast reversible surface Faradaic redox reactions. Particularly, transition metal sulfides have aroused increasing concerns as a novel kind of electrode materials for high-performance pseudocapacitors [16–18]. $NiCo_2S_4$, a binary nickel cobalt sulfide with both nickel and cobalt ions, exhibits much higher electrochemical activity and specific capacitance than its mono-metal sulfides, which results from its good electrical conductivity of about two orders higher than that of its oxide counterparts [19–21]. Therefore, a variety of $NiCo_2S_4$ nanostructures, such as nanoprisms [22], nanotubes [21], hollow spheres [23], and nanowires [24], have been developed to demonstrate excellent electrochemical properties. For example, hollow hexagonal $NiCo_2S_4$ nanoplatelets have been synthesized through a sacrificial template method based on the Kirkendall effect [25], which exhibit a high specific capacitance of 437 F g^{-1} at a current rate of 1 A g^{-1} for supercapacitors. $NiCo_2S_4$ nanotubes prepared by hydrothermal reactions also exhibit a high specific capacitance of 1048 F g^{-1} at the current density of 3.0 A g^{-1} and high capacitance of 75.9% even at the current density of 10.0 A g^{-1} after 5000 charge-discharge cycles [26]. Undoubtedly, construction of novel nanostructured $NiCo_2S_4$ materials can effectively improve the utilization of active materials for their high surface area and shortened electron/ion transport pathways. Nevertheless, caused by their high dependence on surface Faradaic redox reactions and unfavorable reaction kinetics under high current densities, most of $NiCo_2S_4$-based electrode materials still suffer from low rate capability and poor electrochemical stability during the long term charge-discharge processes [27,28]. Furthermore, the serious aggregation tendency of $NiCo_2S_4$ nanoparticles is more likely to cause their severe capacity fading during practical applications. Therefore, it is of essential importance to explore simple but effective strategies to optimize their pseudocapacitive characteristics.

Satisfyingly, conductive carbon materials [29], such as carbon nanotubes [30,31], graphene [32,33], and carbon foam [34], are widely employed as carbonaceous supports for the decoration of nanostructured pseudocapacitive electroactive species due to their high specific surface area, good conductivity, and long cycle life. Compared with carbon nanotubes, graphene, etc, bacterial cellulose (BC) nanofibers have been considered as more promising candidates for the facile synthesis of carbonized BC nanofibers (CBC) on industrial scales due to their competitive superiorities of low cost, environmental friendliness and abundant resource [35–37]. Moreover, incorporation of heteroatoms (*e.g.*, nitrogen) into the carbon lattice has been demonstrated to be an effective strategy to significantly improve the electrical property of carbon materials in our previous works [38,39], thus leading to greatly enhanced rate capability and cycling performance. Herein, BC nanofibers have been used as both template and precursor to fabricate nitrogen-doped carbonized BC nanofibers (CBC-N) and $NiCo_2S_4$ decorated CBC-N composite (CBC-N@$NiCo_2S_4$) as the negative and positive electrode materials for asymmetric supercapacitors (ASCs). Notably, uniformly dispersed $NiCo_2S_4$ nanoparticles are successfully grown on the surface of conductive CBC-N fibers to form CBC-N@$NiCo_2S_4$ composite as an integrated electrode with hierarchical structures and three-dimensional (3D) pathways for fast electrolyte ion diffusion and electron transport. The CBC-N@$NiCo_2S_4$ composite thus obtained exhibits a high specific capacitance of 1078 F g^{-1} at 1 A g^{-1}, a high capacitance retention of 56.4% at 50 A g^{-1}, and an excellent cycling stability of 94.6% retention after 5000 cycles. Moreover, the asymmetric supercapacitor of CBC-N@$NiCo_2S_4$//CBC-N exhibits a wide potential window of 0–1.5 V and a high specific energy of 42.6 Wh kg^{-1} at the power density of 1500 W kg^{-1}, indicating potential applications in high-performance energy storage devices.

2. Experimental section

2.1. Reagents

The bacterial cellulose pellicles (30 × 40 cm^2) were purchased from Hainan Yide Food Co. Ltd. Pyrrole, hexamethylenetetramine (HMT), sodium hydroxide (NaOH), hydrochloric acid (HCl), iron trichloride ($FeCl_3{\cdot}6H_2O$), cobalt nitrate hexahydrate ($Co(NO_3)_2{\cdot}6H_2O$), nickel nitrate ($Ni(NO_3)_2{\cdot}6H_2O$), thiourea (CH_4N_2S), potassium hydroxide (KOH) were all purchased from Sinopharm Chemical Reagent Co. All chemicals were of analytic grade and used without any further purification.

2.2. Preparation of CBC-N nanofibers

The BC pellicles (30 × 40 cm^2) were firstly washed with 0.1 M NaOH solution and deionized water for several times to pH ≈ 7. Then, the raw BC pellicles were cut into rectangular slices (4 × 5 cm^2) to be frozen in liquid nitrogen (−196 °C), and subsequently freeze-dried in a freezer dryer. The freeze-dried BC pellicles (500 mg) were then immerged in 400 mL of 1 mol L^{-1} HCl solution which contains 0.025 M pyrrole monomer. The oxidative polymerization of pyrrole into PPy was carried out at 0 °C by dropwise adding another 400 mL of 1 mol L^{-1} HCl solution containing 0.025 M $FeCl_3{\cdot}6H_2O$. After kept in the ice water bath for 5 h, the product was washed with deionized water for several times to remove the unfixed PPy, thus PPy coated bacterial cellulose composite membrane (denoted as BC/PPy) was obtained. At last, the freeze-dried BC/PPy hybrid membrane was carbonized under Ar atmosphere at 750 °C for 3 h with a heating rate of 5 °C min^{-1} to obtained nitrogen-doped carbon nanofibers, which were named as CBC-N. Carbonized BC nanofibers (denoted as CBC) were also obtained using the same carbonization procedure for comparison.

2.3. Preparation of CBC-N@$NiCo_2S_4$ composite

The growth of $NiCo_2S_4$ on CBC-N was realized via the facile hydrothermal reaction. In a typical procedure, 0.5 mmol of $Ni(NO_3)_2{\cdot}6H_2O$, 1 mmol of $Co(NO_3)_2{\cdot}6H_2O$, 5 mmol of thiourea, and 5 mmol of HMT were added into 30 mL of deionized water and stirred to obtain a light pink solution. Then, 30 mg of CBC-N was dispersed in the above solution and transferred into a 50 mL Teflon-lined stainless-steel autoclave and heated at 160 °C for 12 h (Fig. 1a). After being naturally cooled to room temperature, the final product was rinsed with deionized water for several times and overnight dried at 70 °C, which was named as CBC-N@$NiCo_2S_4$ composite. For comparison, pure $NiCo_2S_4$ powder without CBC-N template was prepared via the same step as shown in Fig. 1b.

2.4. Characterization

Morphology of the samples was observed by field-emission scanning electron microscope (FESEM, Ultra 55, Zeiss) at an accel-

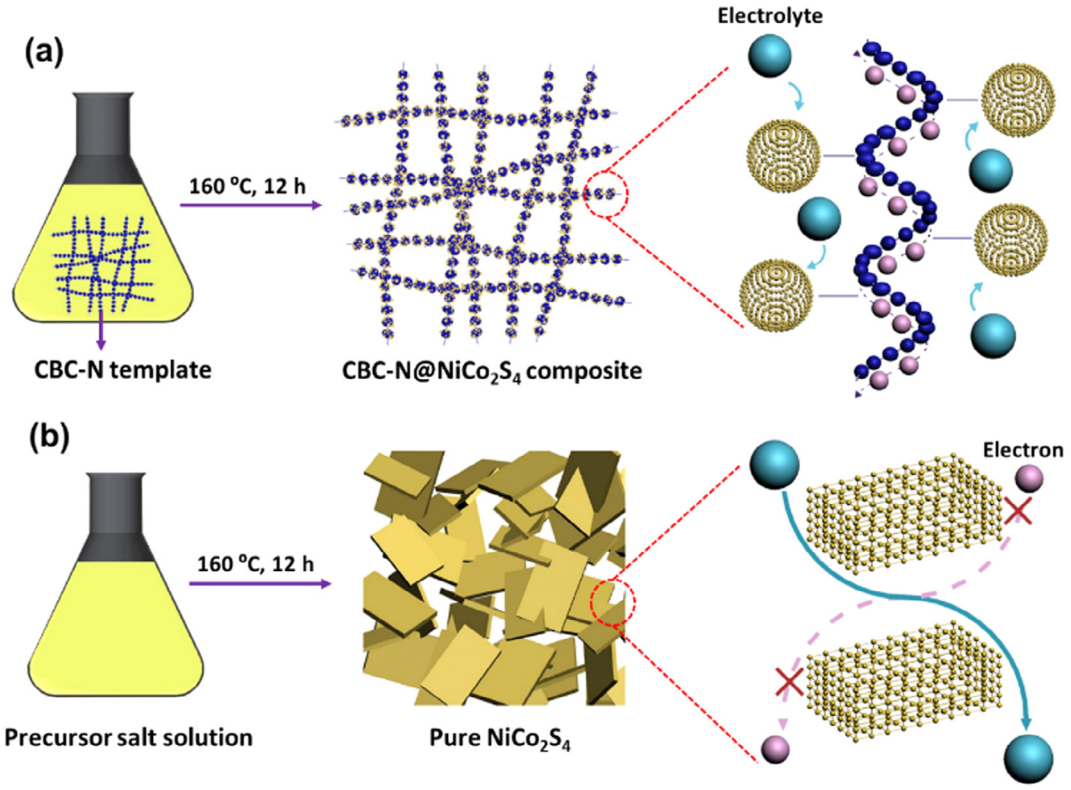

Fig. 1. Schematic illustration of the space-confined growth of CBC-N@$NiCo_2S_4$ composite (a), and the hydrothermal synthesis of $NiCo_2S_4$ in the absence of CNC-N template (b).

eration voltage of 5 kV and transmission electron microscopy (TEM, JEOL-2010) at an acceleration voltage of 200 kV. Phase structures were tested by X-ray diffraction (XRD) patterns (X'Pert PRO, PANalytical) from 5° to 80° at an angular speed (2θ) of 5° min^{-1} with Cu K_α radiation (λ = 0.1542 nm) under a voltage of 40 kV and a current of 40 mA. The chemical composition of CBC-N@$NiCo_2S_4$ composite was examined by energy dispersive X-ray spectroscopy (EDS) and X-ray photoelectron spectroscopy (XPS) with Thermo Scientific ESCALAB 250Xi using an Al K_α sources 1486.6 eV anode. All XPS spectra were corrected according to the C1s line at 284.6 eV, while curve fitting and background subtraction were accomplished using the RBD AugerScan 3.21 software provided by RBD Enterprises. Raman spectra were detected by an inVia Reflex Raman Spectrometer. Brunauer-Emmett-Teller (BET) nitrogen adsorption–desorption isotherms were measured using a Quantachrome Autosorb-iQ/MP®XR system. Thermogravimetric analysis (Pyris 1 TGA, PerkinElmer) was performed in air from 100 to 700 °C at a heating rate of 20 °C min^{-1}. The proportion of $NiCo_2S_4$ in the CBC-N@$NiCo_2S_4$ composite was calculated according to the following equation:

$$P_1 = \frac{W_2 - W_0}{W_1 - W_0} \quad (1)$$

where P_1 is the proportion of $NiCo_2S_4$, W_0 is the weight loss of CBC-N, W_1 is the weight loss of $NiCo_2S_4$, W_2 is the weight loss of CBC-N@$NiCo_2S_4$.

2.5. Eelectrochemical measurements

Electrochemical measurements were conducted in 6 M KOH aqueous solution on an electrochemical working station (CHI600D, Chenhua Instruments Co. Ltd., Shanghai) with a standard three-electrode setup, where Ag/AgCl and Pt wire were used as the reference and counter electrode respectively. Meanwhile, the working electrode was prepared by mixing the milled samples, carbon black and polyvinylidene difluoride in a mass ratio of 80:10:10 to obtain slurry. Then, the slurry was pressed onto the carbon paper current collector at a fixed mass loading of 3 mg and dried at 80 °C for 12 h. cyclic voltammograms (CV) at various scan rates were obtained from −1 to 0 V and −0.1 to 0.5 V for CBC-N nanofibers and CBC-N@$NiCo_2S_4$ composite, respectively. Galvanostatic charge-discharge tests under different current densities were carried out from −1 to 0 V, and 0 to 0.5 V for CBC-N nanofibers and CBC-N@$NiCo_2S_4$ composite, respectively. By applying an AC voltage in the frequency range from 10 mHz to 100 kHz with an amplitude of 5 mV, electrochemical impedance spectroscopy (EIS) measurements were obtained. Specific capacitances (C) of the electrodes are calculated from galvanostatic charge-discharge curves according to the following equation:

$$C = \frac{I \times \Delta t}{m \times V} \quad (2)$$

where I is the current (A), Δt is the discharge time (s), m is the mass of electroactive materials (g), and V is the potential (V).

2.6. Electrochemical measurements of the asymmetric supercapacitor

The asymmetric supercapacitor is assembled by using CBC-N@$NiCo_2S_4$ composite as the positive electrode and CBC-N nanofibers with matched discharge capacity as the negative electrode. The mass ratio of CBC-N@$NiCo_2S_4$ to CBC-N was calculated to be 2.18 according to the following equation:

$$\frac{m_+}{m_-} = \frac{C_- \times V_-}{C_+ \times V_+} \quad (3)$$

where C is the specific capacitance obtained from the three-electrode system (F g^{-1}), V is the potential (V), and m is the mass of the electrode (g).

Energy density and power density of the CBC-N@$NiCo_2S_4$//CBC-N asymmetric supercapacitor were evaluated according to the following equations:

$$P = \frac{E}{\Delta t} \quad (4)$$

$$E = \frac{1}{2} \times C \times V^2 \quad (5)$$

where C is the specific capacitance (F g^{-1}), V is the potential (V), Δt is the discharge time (s), E corresponds to the energy density (Wh kg^{-1}) and P is the power density (W kg^{-1}), respectively.

3. Results and discussion

3.1. Morphology and structure of CBC-N and CBC-N@$NiCo_2S_4$

CBC-N nanofibers are obtained via in-situ polymerization of pyrrole using the raw BC pellicle as template, and subsequent high-temperature carbonization process. As shown in the FESEM images of Fig. 2a and b, a 3D network structure is observed for CBC nanofibers with diameter around 10–30 nm and length up to several micrometers while CBC-N nanofibers show core/sheath structure and "bead-on-string" fiber morphology with the fiber diameter increased to 50 nm. Interestingly, as further indicated in the TEM images (Fig. S1), the 3D nanofibrous network with rough surface is well reserved for CBC-N nanofibers after pyrolysis of BC/PPy composite membrane, which is beneficial to the hydrothermal growth of $NiCo_2S_4$. Moreover, the Raman spectra of CBC and CBC-N fibers (Fig. S2) display two peaks at 1335 and 1585 cm^{-1} corresponding to the characteristic D and G bands of carbon materials, respectively. Since the D band is attributed to the defect and disordered structure of carbon while the G band reflects the crystalline structure of graphitic carbon, the relative intensity ratio of D band to G band (I_D/I_G) in CBC and CBC-N fibers indicates that more disordered structure or defects are generated in CBC-N fibers, which can provide more accessible surface area and increase the charge transfer property during the adsorption process. Therefore, CBC-N nanofibers are considered as the ideal nitrogen-doped carboneous template with good preservation of 3D interconnected networks and appropriate coverage of hierarchically organized carbonized PPy layer. As expected, a much rougher surface and slightly larger fiber diameter can be observed for CBC-N@$NiCo_2S_4$ composite (Fig. 2c). The corresponding EDS elemental mappings (Fig. S3) display the elemental distribution of Ni, Co, S, N and C, indicating the successful and uniform growth of $NiCo_2S_4$ nanoparticles on the CBC-N nanofiber template.

TEM images (Fig. 2d and e) show that $NiCo_2S_4$ nanoparticles are homogeneously and densely distributed on the surface of CBC-N fibers. From the high-resolution TEM (HRTEM) image in Fig. 2e, it can be confirmed that $NiCo_2S_4$ nanoparticles with uniform grain size of 3–5 nm are in close contacts with the amorphous carbon fiber template, implying strong coupling between $NiCo_2S_4$ nanoparticles and CBC-N fibers. Dai et al. have already demonstrated that the direct growth of nanoparticles on oxidized graphene or reduced graphene oxide can afford strong coupling within the hybrid materials, thus leading to optimal electrical and mechanical properties [40]. Fig. 2e also exhibits the lattice fringes with interplanar distances of 0.28 nm and 0.24 nm, corresponding to the (3 1 1) and (4 0 0) planes of $NiCo_2S_4$, respectively [41,42]. For comparison, pure $NiCo_2S_4$ powder with severely aggregated sheet-like structures is obtained in the absence of CBC-N template (Fig. 2f). Therefore, it can be deduced that CBC-N fibers not only play a crucial role in providing nucleation sites for the crystal growth of $NiCo_2S_4$, but also confine the size increase of $NiCo_2S_4$ by its restrained space environment as illustrated in Fig. 1. By incorporating CBC-N fiber template, the severe aggregation of pure $NiCo_2S_4$ nanoparticles can be effectively minimized, thus leading to significantly increased specific surface area. As illustrated by the N_2 adsorption/desorption isotherms and pore size distribution plots in Fig. S4, the surface area of CBC-N@$NiCo_2S_4$ composite reaches 85.2 m^2 g^{-1} with coexisting mesopores and macropores, which can expose more active sites for fast electrolyte diffusion and electron transport.

The XRD pattern of CBC-N@$NiCo_2S_4$ composite (Fig. 3a) shows characteristic peaks at 2θ = 16.3°, 26.8°, 31.6°, 38.3°, 47.4°, 50.5°, and 55.3°, respectively indexed to the (1 1 1), (2 2 0), (3 1 1), (4 0 0), (4 2 2), (5 1 1) and (4 4 0) planes of cubic $NiCo_2S_4$ phase (JCPDS Card No. 20-0782). Meanwhile, the elemental information and oxidation state of CBC-N@$NiCo_2S_4$ composite are identified by XPS. As shown in the survey spectrum (Fig. 3b), peaks at binding energies of 169.7 eV, 781.5 eV, 855.7 eV and 401.1 eV are indexed to S 2p, Co 2p, Ni 2p and N 1s, respectively, indicating the coexistence of S, Co, Ni and N elements in CBC-N@$NiCo_2S_4$ composite.

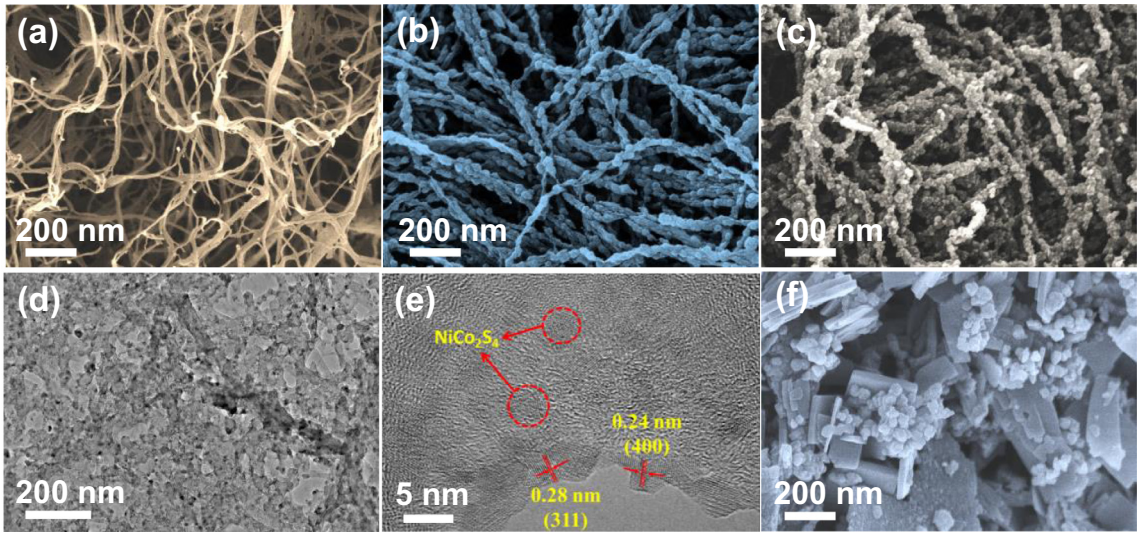

Fig. 2. (a) FESEM images of CBC (a), CBC-N (b), and CBC-N@$NiCo_2S_4$ composite (c). TEM (d) and HRTEM (e) images of CBC-N@$NiCo_2S_4$ composite. FESEM image of pure $NiCo_2S_4$ powder (f).

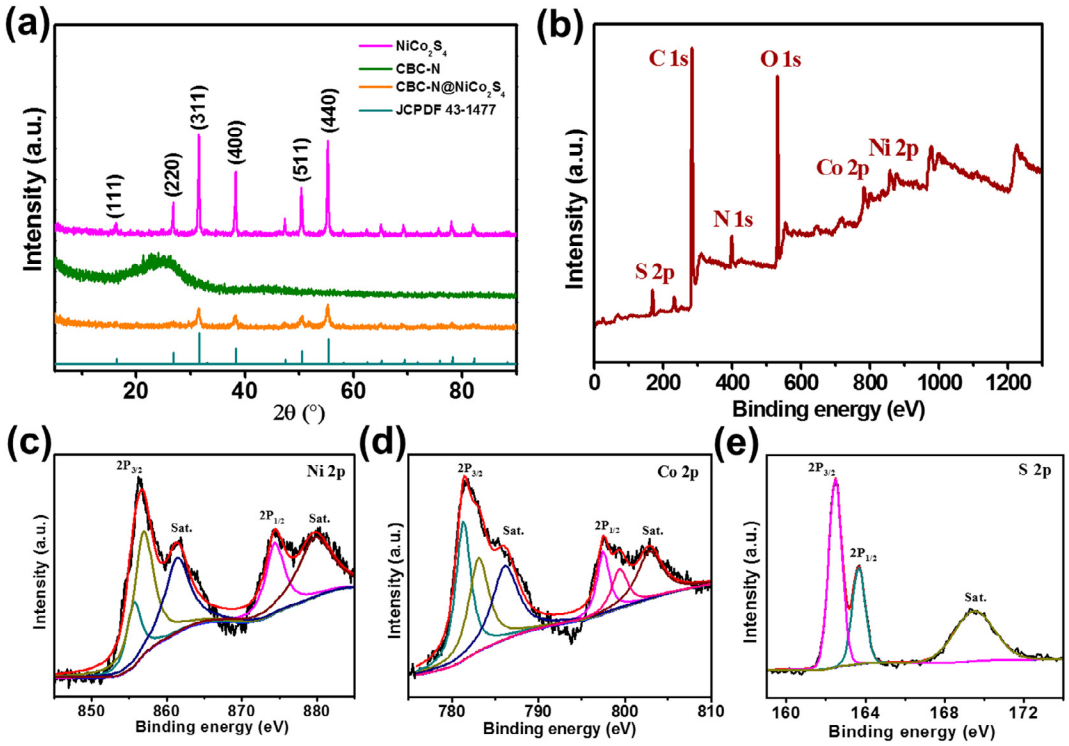

Fig. 3. (a) X-ray diffraction patterns of $NiCo_2S_4$ power, CBC-N nanofibers and CBC-N@$NiCo_2S_4$ composite. XPS spectra of CBC-N@$NiCo_2S_4$ composite: (b) the full survey scan, (c) Ni 2p, (d) Co 2p, and (e) S 2p.

The O element is due to exposure to air. High-resolution Co 2p and Ni 2p spectra are computer fitted by using Gaussian fitting method considering two spin-orbit doublets and two shakeup satellites (marked as "Sat."). The peaks at binding energies of 855.6 eV for Ni $2p_{3/2}$ and 873.1 eV for Ni $2p_{1/2}$ (Fig. 3c) suggest the existence of both Ni^{2+} and Ni^{3+}, while the peaks at binding energies of 781.2 eV for Co $2p_{3/2}$ and 796.5 eV for Co $2p_{1/2}$ (Fig. 3d) demonstrate both Co^{3+} and Co^{2+} in CBC-N@$NiCo_2S_4$ composite. Furthermore, binding energies at 163.6 eV and 162.1 eV in the S 2p spectrum correspond to S $2p_{1/2}$ and S $2p_{3/2}$, respectively (Fig. 3e). Thus, the chemical composition of CBC-N@$NiCo_2S_4$ composite contains Co^{2+}, Co^{3+}, Ni^{2+}, Ni^{3+} and S^{2-}, which are in good agreement with the previously reported results [25,32].

The corresponding loading amount of $NiCo_2S_4$ in the CBC-N@$NiCo_2S_4$ composite is calculated to be 43.5% from the TGA curves as shown in Fig. S5.

3.2. Electrochemical performance of CBC-N and CBC-N@$NiCo_2S_4$

Electrochemical performance of CBC and CBC-N fibers is evaluated using a standard three electrode system in 6 M KOH aqueous electrolyte. As observed in Fig. 4a, both CBC and CBC-N fibers show quasi-rectangle CV curves, indicating ideal double-layer capacitance behaviors. Moreover, the integrated area for the CV curve of CBC-N is much larger than that of CBC at the same scan rate of 20 mV s^{-1}, indicating much higher capacitive performance of CBC-N fibers due to more active sites provided by the abundant nitrogen-containing functional groups for electric double layer formation and Faradic redox reactions [38,43,44]. In addition, the quasi-rectangle CV curves are well maintained between −1 and 0 V for CBC-N fibers with increasing scan rate (Fig. 4b), implying its good rate performance. Fig. 4c shows the galvanostatic charge-discharge curves of CBC-N fibers under different current densities, which exhibit nearly linear and symmetrical triangle shapes, further implying the ideal double layer capacitive characteristic and excellent electrochemical reversibility. Moreover, the specific capacitances of CBC-N and CBC fibers as a function of the current densities (Fig. 4d) are respectively calculated from their discharge curves as shown in Figs. 4c and S6c. A high specific capacitance of 377.8 F g^{-1} can be achieved for CBC-N fibers, being much higher than that (231.0 F g^{-1}) of CBC fibers at the same current density of 1 A g^{-1}. The superior capacitive performance of CBC-N fibers can be attributed to the well-organized 3D conductive network derived from bacterial cellulose and nitrogen-doped "bead-on-string" structure with increased surface active sites for fast electrolyte diffusion and electron transport.

Considering that the energy and power densities of asymmetric supercapacitors highly depend on the electrochemical properties of positive electrode materials, CBC-N@$NiCo_2S_4$ composite is obtained via the hydrothermal growth of $NiCo_2S_4$ by using CBC-N fibers as the conductive template. As shown in Fig. 5a, well-defined redox peaks can be observed in the CV curves of CBC-N@$NiCo_2S_4$ composite and $NiCo_2S_4$ powder. These distinct peaks can be attributed to the Faradaic redox reactions between the electrode materials and alkaline electrolyte according to the following equations [45,46]:

$$CoS + OH^- \leftrightarrow CoSOH + e^- \quad (6)$$

$$CoSOH + OH^- \leftrightarrow CoSO + H_2O + e^- \quad (7)$$

$$NiS + OH^- \leftrightarrow NiSOH + e^- \quad (8)$$

Moreover, the integrated area for the CV curve of CBC-N@$NiCo_2S_4$ composite is much larger than those of pure $NiCo_2S_4$ and CBC-N nanofibers under the same scan rate of 20 mV s^{-1}, revealing better pseudocapacitive characteristics of CBC-N@$NiCo_2S_4$ composite than pure $NiCo_2S_4$ and CBC-N nanofibers. This is mainly ascribed to the uniformly anchored $NiCo_2S_4$ nanoparticles on the CBC-N fiber template. As shown in Fig. 1a, electron transfer pathways can be effectively built up by the

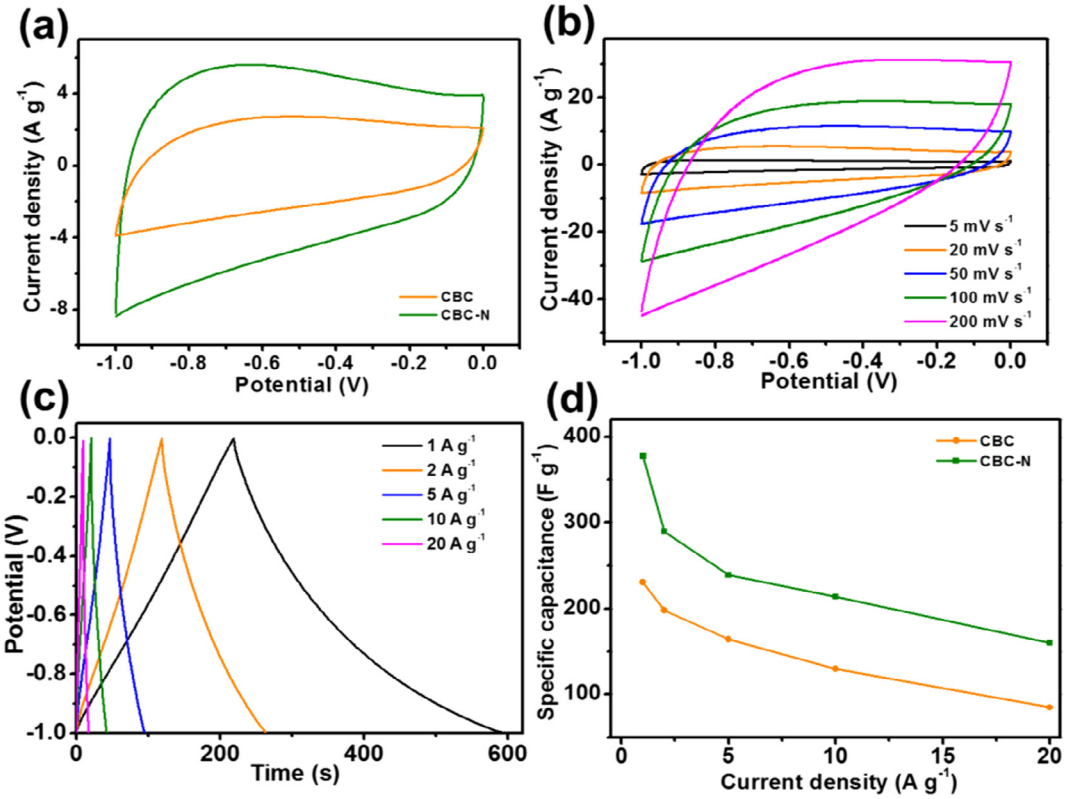

Fig. 4. (a) CV curves of CBC and CBC-N nanofibers at a scan rate of 20 mV s^{-1}; (b) CV curves of CBC-N nanofibers at various scan rates; (c) Galvanostatic charge-discharge curves at various current densities for CBC-N nanofibers; (d) Specific capacitances of CBC-N and CBC nanofibers at various current densities.

three-dimensionally interconnected CBC-N nanofibers while they may be cut off between individual $NiCo_2S_4$ nanoparticle without the CBC-N nanofiber template (Fig. 1b). Furthermore, benefitting from the effective coupling between $NiCo_2S_4$ nanoparticles and highly conductive CBC-N nanofibers, the anodic peaks only slightly shift to higher potential while the cathodic peaks shift to lower potential for CBC-N@$NiCo_2S_4$ composite with the scan rate increased from 5 to 200 mV s^{-1} as shown in Fig. 5b. The galvanostatic charge-discharge curves of CBC-N@$NiCo_2S_4$ composite (Fig. 5c) also show symmetric charge and discharge processes with very small voltage drops even under high current densities, indicating the excellent electrical and ionic conductivity of CBC-N@$NiCo_2S_4$ composite as pseudocapacitor electrodes. Specific capacitances of CBC-N@$NiCo_2S_4$ composite and pure $NiCo_2S_4$ powder as a function of the current densities (Fig. 5d) are respectively plotted based on their discharge curves in Figs. 5c and S6d. Compared with pure $NiCo_2S_4$, the specific capacitance (1078 F g^{-1} at 1 A g^{-1}) of CBC-N@$NiCo_2S_4$ composite is greatly improved, compared with that (479.7 F g^{-1}) of pure $NiCo_2S_4$. Moreover, the specific capacitance of CBC-N@$NiCo_2S_4$ composite is 1053, 988, 912, 813 and 608 F g^{-1} under current density of 2, 5, 10, 20 and 50 A g^{-1}, respectively. That is to say, the capacitance retentions still remain as high as 75.4% and 56.4% for CBC-N@$NiCo_2S_4$ composite even at relatively high current densities of 20 and 50 A g^{-1}, respectively. These values are superior to most of the previously reported nickel-cobalt sulfide based electrode materials as shown in Table S1. Besides, the CBC-N@$NiCo_2S_4$ electrode possesses good cycling stability with a high capacity retention of 94.6% (918.5 F g^{-1} at 5 A g^{-1}) after 5000 cycles due to the excellent stability of CBC-N template (Fig. 5e), which can fully meet the commercial requirements of pseudocapacitors. It has been indicated that there is almost no significant change in the morphology of CBC-N@$NiCo_2S_4$ electrode after the cycling test (Fig. S7). For comparison, the cycling stability of pure $NiCo_2S_4$ powder is also obtained with a poor capacitance retention of 77.5% at current density of 5 A g^{-1}.

To further investigate the electrochemical impedance of CBC-N, $NiCo_2S_4$ and CBC-N@$NiCo_2S_4$ composite, Nyquist plots at open-circuit potentials in the frequency range from 100 kHz to 0.01 Hz are provided as shown in Fig. 5f. No obvious semicircle is observed for all of the above electrodes during the high charge transfer process, while the vertical slopes in the low frequency region demonstrate lower resistance of CBC-N@$NiCo_2S_4$ composite over $NiCo_2S_4$ powder. All these results further demonstrate the illustration as shown in Fig. 1: (1) The highly conductive CBC fiber template derived from bacterial cellulose effectively builds up a 3D architecture that allows easy electrolyte access and electron transfer; (2) The "bead-on-string" fiber morphology of CBC-N fibers after the effective nitrogen-doping can provide more surface active sites for in-situ growth of $NiCo_2S_4$, and enhance the capacitance of CBC fibers by introducing Faradaic interactions between electrolyte ions and nitrogen-doped carbon electrode surface as well; (3) The highly dispersed $NiCo_2S_4$ nanoparticles with size of only 3–5 nm on the surface of CBC-N template can afford more active sites exposed to the electrolyte, thus leading to fast charge transportation and large increment of the specific capacitance.

3.3. Electrochemical performance of the asymmetric supercapacitor

To evaluate the electrochemical performance of CBC-N@$NiCo_2S_4$ composite for potential energy storage applications, an asymmetric supercapacitor of CBC-N@$NiCo_2S_4$//CBC-N is fabricated by using CBC-N@$NiCo_2S_4$ composite as the positive electrode and CBC-N fibers as the negative electrode (Fig. 6a). Fig. 6b shows the corresponding CV curves of the assembled asymmetric supercapacitor under different scan rates. It can be seen that the stable electro-

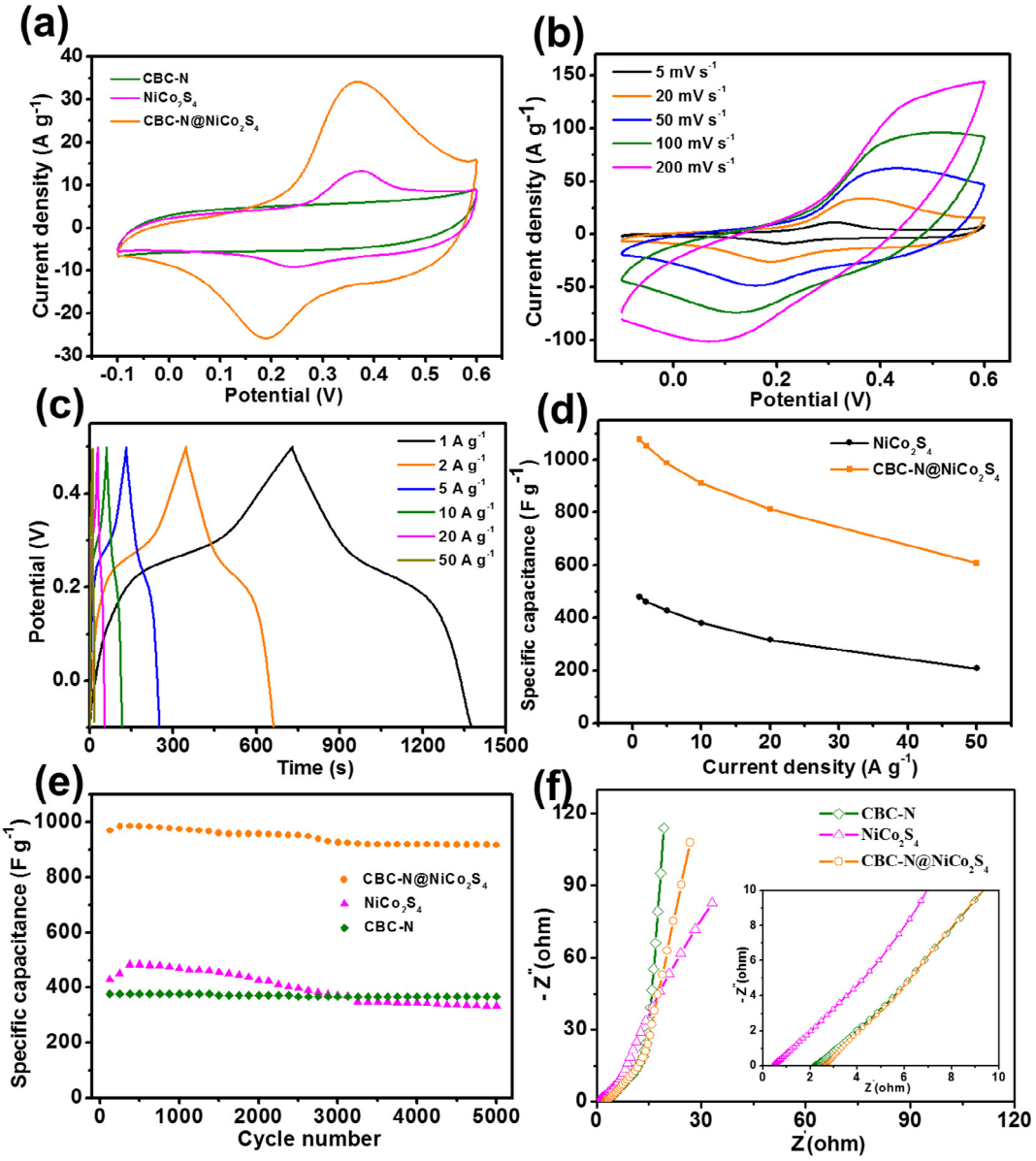

Fig. 5. (a) CV curves of CBC-N, $NiCo_2S_4$ powder and CBC-N@$NiCo_2S_4$ composite at a scan rate of 20 mV s^{-1}; (b) CV curves of CBC-N@$NiCo_2S_4$ composite at various scan rates; (c) Galvanostatic charge-discharge curves at various current densities for CBC-N@$NiCo_2S_4$ composite; (d) Specific capacitances of $NiCo_2S_4$ powder and CBC-N@$NiCo_2S_4$ composite at various current densities; (e) The long-term cycling performance of CBC-N, $NiCo_2S_4$ and CBC-N@$NiCo_2S_4$ at a current density of 5 A g^{-1}; (f) Nyquist plots of CBC-N, $NiCo_2S_4$ and CBC-N@$NiCo_2S_4$ electrode materials. The inset shows the corresponding Nyquist plots at high-frequency region.

chemical window of CBC-N@$NiCo_2S_4$//CBC-N can be extended to 1.5 V with both electrical double layer capacitance and pseudocapacitance characteristics. Moreover, the CV curve of the asymmetric supercapacitor has no obvious distortion even under a high scan rate of 100 mV s^{-1}. Galvanostatic charge-discharge curves of the assembled asymmetric supercapacitor device at different current densities are shown in Fig. 6c. According to Eq. (2), the specific capacitances are calculated to be 136.7, 107.7 and 75.3 F g^{-1} respectively at current densities of 2, 5 and 10 A g^{-1} for the CBC-N@$NiCo_2S_4$//CBC-N asymmetric supercapacitor (Fig. 6d). Consequently, the corresponding Ragone plots of the asymmetric supercapacitor (Fig. 6e) are calculated from the galvanostatic discharge curves based on Eqs. (4) and (5).

The CBC-N@$NiCo_2S_4$//CBC-N asymmetric supercapacitor exhibits high energy density of 42.6 Wh kg^{-1} at the power density of 1500 W kg^{-1}, and still remains high energy density of 23.5 Wh kg^{-1} at the power density of 7500 W kg^{-1}, which is much higher than those of previously reported nickel and cobalt-based asymmetric supercapacitors including Ni_xCo_{1-x}LDH-Zn_2SnO_4// activated carbon (23.7 Wh kg^{-1} at a power density of 284.2 W kg^{-1}) [47], $NiCo_2S_4$ nanotube arrays on Ni foam//reduced graphene oxide (31.5 Wh kg^{-1} at a power density of 156.6 W kg^{-1}) [21], nickel cobaltite-graphene//activated carbon (19.5 Wh kg^{-1} at 100 W kg^{-1}) [48], $NiCo_2S_4$ grown on Ni foam//activated carbon (33.9 Wh kg^{-1} at 409 W kg^{-1}) [49], $NiCo_2S_4$ nanosheets//activated carbon (25.5 Wh kg^{-1} at 334 W kg^{-1}) [50], Ni-Co sulfide nanowire arrays//activated carbon (25 Wh kg^{-1} at 3570 W kg^{-1}) [24], $NiCo_2S_4$@$Co(OH)_2$ nanotube arrays supported on Ni foam//activated carbon (35.89 Wh kg^{-1} at 400 W kg^{-1}) [51], $NiCo_2(CO_3)_{1.5}(OH)_3$@$NiCo_2S_4$//activated carbon (32.3 Wh kg^{-1} at 1835 W kg^{-1}) [52] and $NiCo_2O_4$@NiO//activated carbon (31.5 Wh kg^{-1} at 215.2 W kg^{-1}) [53]. Meanwhile, the low resistance shown in the Nyquist plot of the asymmetric supercapacitor (Fig. S8) further indicates its rapid electron transfer process during

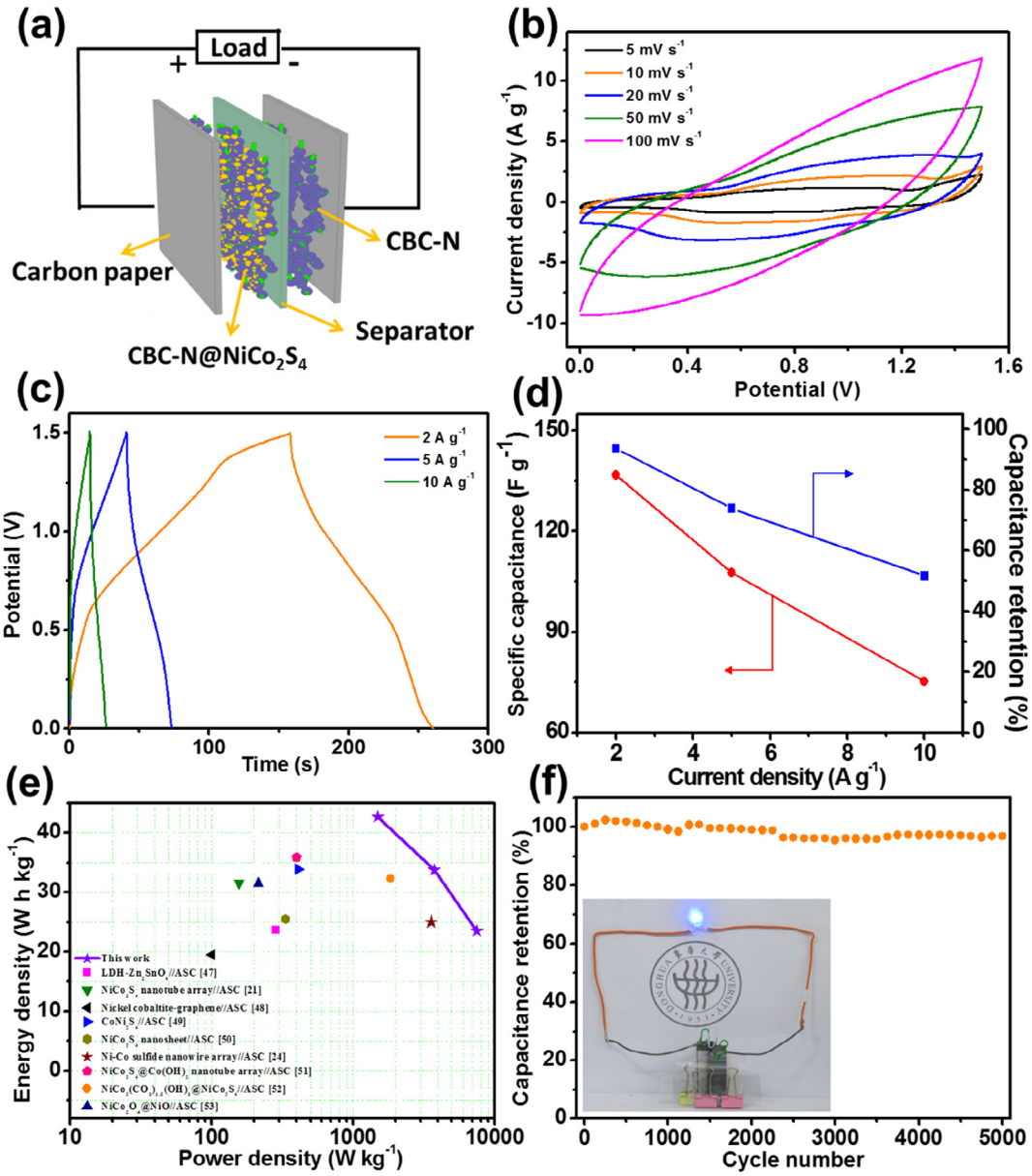

Fig. 6. (a) Schematic of the assembled structure of an asymmetric supercapacitor based on CBC-N@$NiCo_2S_4$ composite as the positive electrode material and CBC-N nanofibers as the negative electrode material; CV curves at various scan rates (b) and galvanostatic charge-discharge curves at various current densities (c) for the assembled asymmetric supercapacitor; (d) Specific capacitance and the corresponding capacitance retention of the as-assembled CBC-N@$NiCo_2S_4$//CBC-N ASC device at different current densities; (e) Ragone plots of the as-assembled ASC device and recently reported values for comparison; (f) The long-term cycling performance of the device at a current density of 5 A g^{-1} (The inset shows a blue LED lighted up by using two series of CBC-N@$NiCo_2S_4$//CBC-N asymmetric supercapacitors). (For interpretation of the references to colour in this figure legend, the reader is referred to the web version of this article.)

charge-discharge reactions. The CBC-N@ $NiCo_2S_4$//CBC-N device also exhibits good electrochemical stability with approximately 96.8% retention of its initial specific capacitance at 5 A g^{-1} after 5000 cycles (Fig. 6f), which indicates the potential applications of CBC-N@ $NiCo_2S_4$//CBC-N asymmetric supercapacitors in energy storage devices. From the inset of Fig. 6f, it can be observed that a blue LED with a voltage of 3 V can be lighted up by using two series of our CBC-N@ $NiCo_2S_4$//CBC-N asymmetric supercapacitors which have been fully charged for 20 s at 3.0 V.

4. Conclusions

In summary, both nitrogen-doped carbon nanofibers (CBC-N) and $NiCo_2S_4$ decorated CBC-N (CBC-N@$NiCo_2S_4$) composite electrodes have been fabricated for asymmetric supercapacitor applications by using bacterial cellulose nanofibers as template and precursor. Benefiting from the spaced-confined hydrothermal growth of $NiCo_2S_4$, and strong coupling between uniformly dispersed $NiCo_2S_4$ nanoparticles and the highly conductive CBC-N template, CBC-N@$NiCo_2S_4$ composite can supply more active sites to allow fast electrolyte diffusion and electron transfer. Therefore, the assembled CBC-N@$NiCo_2S_4$//CBC-N asymmetric supercapacitor can operate under a wide potential window of 0–1.5 V with high specific energy of 42.6 Wh kg^{-1} at the power density of 1500 W kg^{-1}. More importantly, the long cycling stability of CBC-N@$NiCo_2S_4$//CBC-N asymmetric supercapacitor opens up new possibilities for fabricating high-performance energy storage devices with high flexibility, lightweight, excellent specific energy and power performance.

Acknowledgements

The authors are grateful for the financial support from the National Natural Science Foundation of China (51373037, 51433001), Program of Shanghai Academic Research Leader (17XD1400100), Guangxi Small Highland Innovation Team of Talents in Colleges and Universities, Guangxi Funds for Specially-appointed Expert, and Guangxi Natural Science Foundation of China (No. 2014GXNSFAA118321).

Appendix A. Supplementary data

Supplementary data associated with this article can be found, in the online version, at http://dx.doi.org/10.1016/j.cej.2017.07.062.

References

[1] A.L.M. Reddy, S.R. Gowda, M.M. Shaijumon, P.M. Ajayan, Hybrid nanostructures for energy storage applications, Adv. Mater. 24 (2012) 5045–5064.
[2] X.H. Lu, M.H. Yu, G.M. Wang, Y.X. Tong, Y. Li, Flexible solid-state supercapacitors: design, fabrication and applications, Energy Environ. Sci. 7 (2014) 2160–2181.
[3] G.P. Wang, L. Zhang, J.J. Zhang, A review of electrode materials for electrochemical supercapacitors, Chem. Soc. Rev. 41 (2012) 797–828.
[4] S. Chen, W. Xing, J.J. Duan, X.J. Hu, S.Z. Qiao, Nanostructured morphology control for efficient supercapacitor electrodes, J. Mater. Chem. A 1 (2013) 2941–2954.
[5] P. Simon, Y. Gogotsi, Materials for electrochemical capacitors, Nat. Mater. 7 (2008) 845–854.
[6] J.P. Liu, J. Jiang, C.W. Cheng, H.X. Li, J.X. Zhang, H. Gong, H.J. Fan, Co_3O_4 nanowire@MnO_2 ultrathin nanosheet core/shell arrays: a new class of high-performance pseudocapacitive materials, Adv. Mater. 23 (2011) 2076–2081.
[7] C.Z. Yuan, J.Y. Li, L.R. Hou, X.G. Zhang, L.F. Shen, X.W. Lou, Ultrathin mesoporous $NiCo_2O_4$ nanosheets supported on Ni foam as advanced electrodes for supercapacitors, Adv. Funct. Mater. 22 (2012) 4592–4597.
[8] J.F. Xie, X. Sun, N. Zhang, K. Xu, M. Zhou, Y. Xie, Layer-by-layer β-Ni$[OH]_2$/graphene nanohybrids for ultraflexible all-solid-state thin-film supercapacitors with high electrochemical performance, Nano Energy 2 (2013) 65–74.
[9] L.Q. Mai, F. Yang, Y.L. Zhao, X. Xu, L. Xu, Y.Z. Luo, Hierarchical $MnMoO_4$/$CoMoO_4$ heterostructured nanowires with enhanced supercapacitor performance, Nat. Commun. 2 (2011) 381.
[10] J.H. Zhao, M.B. Zheng, Z. Run, J. Xia, M.J. Sun, H. Pang, 1D $Co_{2.18}Ni_{0.82}Si_2O_5(OH)_4$ architectures assembled by ultrathin nanoflakes for high-performance flexible solid-state asymmetric supercapacitors, J. Power Sources 285 (2015) 385–392.
[11] C.Z. Wei, C. Cheng, L. Ma, M.N. Liu, D.C. Kong, W.M. Du, H. Pang, Mesoporous hybrid NiO_x-MnO_x nanoprisms for flexible solid-state asymmetric supercapacitors, Dalton Trans. 45 (2016) 10789–10797.
[12] H. Pang, X.R. Li, Q.X. Zhao, H.G. Xue, W.Y. Lai, Z. Hu, W. Huang, One-pot synthesis of heterogeneous Co_3O_4-nanocube/$Co(OH)_2$-nanosheet hybrids for high-performance flexible asymmetric all-solid-state supercapacitors, Nano Energy 35 (2017) 138–145.
[13] H.J. Tang, J.Y. Wang, H.J. Yin, H.J. Zhao, D. Wang, Z. Tang, Growth of polypyrrole ultrathin films on MoS_2 monolayers as high-performance supercapacitor electrodes, Adv. Mater. 27 (2015) 1117–1123.
[14] C. Zhou, Y.W. Zhang, Y.Y. Li, J.P. Liu, Construction of high-capacitance 3D CoO@polypyrrole nanowire array electrode for aqueous asymmetric supercapacitor, Nano Lett. 13 (2013) 2078–2085.
[15] H.M. Zhang, X.H. Wang, Eco-friendly water-borne conducting polyaniline, Chinese J. Polym. Sci. 31 (2013) 853–869.
[16] W.H. Cai, T. Lai, J.W. Lai, H.T. Xie, L.Z. Ouyang, J.S. Ye, C.Z. Yu, Transition metal sulfides grown on graphene fibers for wearable asymmetric supercapacitors with high volumetric capacitance and high energy density, Sci. Rep. 6 (2016) 26890.
[17] X. Hu, W. Shao, X.D. Hang, X.D. Zhang, W.G. Zhu, Y. Xie, Superior electrical conductivity in hydrogenated layered ternary chalcogenide nanosheets for flexible all-solid-state supercapacitors, Angew. Chem. Int. Ed. 55 (2016) 5733–5738.
[18] X. Xu, Z.Y. Fan, S.J. Ding, D.M. Yu, Y.P. Du, Fabrication of MoS_2 nanosheet@TiO_2 nanotube hybrid nanostructures for lithium storage, Nanoscale 6 (2014) 5245–5250.
[19] B. Li, M.B. Zheng, H.G. Xue, H. Pang, High performance electrochemical capacitor materials focusing on nickel based materials, Inorg. Chem. Front. 3 (2016) 175–202.
[20] W. Chen, C. Xia, H.N. Alshareef, One-step electrodeposited nickel cobalt sulfide nanosheet arrays for high-performance asymmetric supercapacitors, ACS Nano 8 (2014) 9531–9541.
[21] H.C. Chen, J.J. Jiang, L. Zhang, D.D. Xia, Y.D. Zhao, D.Q. Guo, T. Qi, H.Z. Wan, In situ growth of $NiCo_2S_4$ nanotube arrays on Ni foam for supercapacitors: maximizing utilization efficiency at high mass loading to achieve ultrahigh areal pseudocapacitance, J. Power Sources 254 (2014) 249–257.
[22] L. Yu, L. Zhang, H.B. Wu, X.W. Lou, Formation of $NixCo_{3-x}S_4$ hollow nanoprisms with enhanced pseudocapacitive properties, Angew. Chem. Int. Ed. 53 (2014) 3711–3714.
[23] L.F. Shen, L. Yu, H.B. Wu, X.Y. Yu, X.G. Zhang, X.W. Lou, Formation of nickel cobalt sulfide ball-in-ball hollow spheres with enhanced electrochemical pseudocapacitive properties, Nat. Commun. 6 (2015) 6694.
[24] Y.H. Li, L.J. Cao, L. Qiao, M. Zhou, Y. Yang, P. Xiao, Y.H. Zhang, Ni-Co sulfide nanowires on nickel foam with ultrahigh capacitance for asymmetric supercapacitors, J. Mater. Chem. A 2 (2014) 6540–6548.
[25] J. Pu, F.L. Cui, S.B. Chu, T.T. Wang, E.H. Sheng, Z.H. Wang, Preparation and electrochemical characterization of hollow hexagonal $NiCo_2S_4$ nanoplates as pseudocapacitor materials, ACS Sustain. Chem. Eng. 2 (2014) 809–815.
[26] Y.F. Zhang, M.Z. Ma, J. Yang, C.C. Sun, H.Q. Su, W. Huang, X.C. Dong, Shape-controlled synthesis of $NiCo_2S_4$ and their charge storage characteristics in supercapacitors, Nanoscale 6 (2014) 9824–9830.
[27] D. Li, R.B. Kaner, How nucleation affects the aggregation of nanoparticles, J. Mater. Chem. 17 (2007) 2279–2282.
[28] A.S. Arico, P. Bruce, B. Scrosati, J.M. Tarascon, W. van Schalkwijk, Nanostructured materials for advanced energy conversion and storage devices, Nat. Mater. 4 (2005) 366–377.
[29] Z.N. Yu, L. Tetard, L. Zhai, J. Thomas, Supercapacitor electrode materials: nanostructures from 0 to 3 dimensions, Energy Environ. Sci. 8 (2015) 702–730.
[30] S. Nardecchia, D. Carriazo, M.L. Ferrer, M.C. Gutierrez, F. del Monte, Three dimensional macroporous architectures and aerogels built of carbon nanotubes and/or graphene: synthesis and applications, Chem. Soc. Rev. 42 (2013) 794–830.
[31] X. Xu, D.M. Yu, H. Zhou, L.S. Zhang, C.H. Xiao, C.W. Guo, S.W. Guo, S.J. Ding, MoS_2 nanosheets grown on amorphous carbon nanotubes for enhanced sodium storage, J. Mater. Chem. A 4 (2016) 4375–4379.
[32] X.L. Wu, L.L. Jiang, C.L. Long, T. Wei, Z.J. Fan, Dual support system ensuring porous Co-Al hydroxide nanosheets with ultrahigh rate performance and high energy density for supercapacitors, Adv. Funct. Mater. 25 (2015) 1648–1655.
[33] B.T. Dong, H. Zhou, J. Liang, L.S. Zhang, G.X. Gao, S.J. Ding, One-step synthesis of free-standing α-Ni$[OH]_2$ nanosheets on reduced graphene oxide for high-performance supercapacitors, Nanotechnology 25 (2014) 435403.
[34] L.F. Shen, J. Wang, G.Y. Xu, H.S. Li, H. Dou, X.G. Zhang, $NiCo_2S_4$ nanosheets grown on nitrogen-doped carbon foams as an advanced electrode for supercapacitors, Adv. Energy Mater. 5 (2015) 1400977.
[35] L.F. Chen, Z.H. Huang, H.W. Liang, Q.F. Guan, S.H. Yu, Bacterial-cellulose-derived carbon nanofiber@MnO_2 and nitrogen-doped carbon nanofiber electrode materials: An asymmetric supercapacitor with high energy and power density, Adv. Mater. 25 (2013) 4746–4752.
[36] C.L. Long, D.P. Qi, T. Wei, J. Yan, L.L. Jiang, Z.J. Fan, Nitrogen-doped carbon networks for high energy density supercapacitors derived from polyaniline coated bacterial cellulose, Adv. Funct. Mater. 24 (2014) 3953–3961.
[37] L.F. Chen, Z.H. Huang, H.W. Liang, W.T. Yao, Z.Y. Yu, S.H. Yu, Flexible all-solid-state high-power supercapacitor fabricated with nitrogen-doped carbon nanofiber electrode material derived from bacterial cellulose, Energy Environ. Sci. 6 (2013) 3331–3338.
[38] F.L. Lai, Y.E. Miao, L.Z. Zuo, H.Y. Lu, Y.P. Huang, T.X. Liu, Biomass-derived nitrogen-doped carbon nanofiber network: a facile template for decoration of ultrathin nickel-cobalt layered double hydroxide nanosheets as high-performance asymmetric supercapacitor electrode, Small 12 (2016) 3235–3244.
[39] W. Fan, Y.Y. Xia, W.W. Tjiu, P.K. Pallathadka, C.B. He, T.X. Liu, Nitrogen-doped graphene hollow nanospheres as novel electrode materials for supercapacitor applications, J. Power Sources 243 (2013) 973–981.
[40] Y.Y. Liang, Y.G. Li, H.L. Wang, H.J. Dai, Strongly coupled inorganic/nanocarbon hybrid materials for advanced electrocatalysis, J. Am. Chem. Soc. 135 (2013) 2013–2036.
[41] M. Sun, J.J. Tie, G. Cheng, T. Lin, S.M. Peng, F.Z. Deng, F. Ye, L. Yu, In situ growth of burl-like nickel cobalt sulfide on carbon fibers as high-performance supercapacitors, J. Mater. Chem. A 3 (2015) 1730–1736.
[42] H.C. Chen, J.J. Jiang, L. Zhang, H.Z. Wan, T. Qi, D.D. Xia, Highly conductive $NiCo_2S_4$ urchin-like nanostructures for high-rate pseudocapacitors, Nanoscale 5 (2013) 8879–8883.
[43] C.N.R. Rao, K. Gopalakrishnan, A. Govindaraj, Synthesis, properties and applications of graphene doped with boron, nitrogen and other elements, Nano Today 9 (2014) 324–343.
[44] Y.Y. Wen, C.C. Huang, L.Z. Wang, D. Hulicova Jurcakova, Heteroatom-doped graphene for electrochemical energy storage, Chin. Sci. Bull. 59 (2014) 2102–2121.
[45] W. Kong, C.C. Lu, W. Zhang, J. Pu, Z.H. Wang, Homogeneous core-shell $NiCo_2S_4$ nanostructures supported on nickel foam for supercapacitors, J. Mater. Chem. A 3 (2015) 12452–12460.
[46] J.W. Xiao, L. Wan, S.H. Yang, F. Xiao, S. Wang, Design hierarchical electrodes with highly conductive $NiCo_2S_4$ nanotube arrays grown on carbon fiber paper for high-performance pseudocapacitors, Nano Lett. 14 (2014) 831–838.
[47] X. Wang, A. Sumboja, M. Lin, J. Yan, P.S. Lee, Enhancing electrochemical reaction sites in nickel-cobalt layered double hydroxides on zinc tin oxide nanowires: a hybrid material for an asymmetric supercapacitor device, Nanoscale 4 (2012) 7266–7272.
[48] H.L. Wang, C.M.B. Holt, Z. Li, X.H. Tan, B.S. Amirkhiz, Z.W. Xu, B.C. Olsen, T. Stephenson, D. Mitlin, Graphene-nickel cobaltite nanocomposite asymmetrical

supercapacitor with commercial level mass loading, Nano Res. 5 (2012) 605–617.
[49] W. Hu, R.Q. Chen, W. Xie, L.L. Zou, N. Qin, D.H. Bao, $CoNi_2S_4$ nanosheet arrays supported on nickel foams with ultrahigh capacitance for aqueous asymmetric supercapacitor applications, ACS Appl. Mater. Interfaces 6 (2014) 19318–19326.
[50] Z.B. Wu, X.L. Pu, X.B. Ji, Y.R. Zhu, M.J. Jing, Q.Y. Chen, F.P. Jiao, High energy density asymmetric supercapacitors from mesoporous $NiCo_2S_4$ nanosheets, Electrochim. Acta 174 (2015) 238–245.
[51] R. Li, S.L. Wang, Z.C. Huang, F.X. Lu, T.B. He, $NiCo_2S_4$@$Co(OH)_2$ core-shell nanotube arrays in situ grown on Ni foam for high performances asymmetric supercapacitors, J. Power Sources 312 (2016) 156–164.
[52] B. Yang, L. Yu, H.J. Yan, Y.B. Sun, Q. Liu, J.Y. Liu, D.L. Song, S.X. Hu, Y. Yuan, L.H. Liu, Fabrication of urchin-like $NiCo_2(CO_3)_{1.5}(OH)_3$@$NiCo_2S_4$ on Ni foam by an ion-exchange route and application to asymmetrical supercapacitors, J. Mater. Chem. A 3 (2015) 13308–13316.
[53] X.J. Liu, J.F. Liu, X.M. Sun, $NiCo_2O_4$@NiO hybrid arrays with improved electrochemical performance for pseudocapacitors, J. Mater. Chem. A 3 (2015) 13900–13905.